

Forward Modeling Galaxy Size in a Cosmological Context

Andrew Hearin¹, Peter Behroozi², Andrey Kravtsov³, Benjamin Moster⁴

¹*Argonne National Laboratory, Argonne, IL, USA 60439, USA*

²*Department of Physics, University of Arizona, 1118 E 4th St, Tucson, AZ 85721 USA*

³*Department of Astronomy & Astrophysics, The University of Chicago, Chicago, IL 60637 USA*

⁴*Universitäts-Sternwarte, Ludwig-Maximilians-Universität München, Scheinerstr. 1, 81679 München, Germany*

3 October 2017

ABSTRACT

We derive empirical modeling constraints on the connection between dark matter halos and the half-light radius of galaxies, $R_{1/2}$. Novel to this work, we study galaxy size using new SDSS measurements of the $R_{1/2}$ –dependence of galaxy clustering. Smaller galaxies cluster stronger relative to larger galaxies of the same stellar mass, a new result. We use **Halotools** to test a collection of forward models of galaxy size to identify the qualitative ingredients needed to reproduce the observed clustering. We show that the $R_{1/2}$ –dependence of galaxy clustering is largely driven by centrals being larger than satellite galaxies of the same halo mass. Models in which $R_{1/2}$ is determined by stellar mass M_* exhibit qualitatively discrepant clustering properties from SDSS galaxies. Models where $R_{1/2}$ is linearly proportional to halo virial radius R_{vir} at the time of peak halo mass are much more successful, provided that scatter in $R_{1/2}$ is significantly correlated with the halo scale radius R_s at that time. Together with the result that stellar mass stripping of satellites has only a mild impact on $R_{1/2}$ –dependent clustering, this suggests that the relative size of centrals and satellites is already in place at the time of satellite infall, and supports the notion that L_* galaxy and halo profiles co-evolve across many Gyr of cosmic time.

1 INTRODUCTION

Some introduction goes here.

2 DATA AND SIMULATIONS

Our galaxy sample comes from the catalog of SDSS galaxy profile decompositions provided by Meert et al. (2015). This catalog is based on Data Release 10 of the Sloan Digital Sky Survey (SDSS, Ahn et al. 2014), with improvements to the photometry pipeline and light profile fitting methods (Vikram et al. 2010; Bernardi et al. 2013, 2014; Meert et al. 2013). In the version of this catalog that we use, two-dimensional r –band profiles were fit with a two-component de Vaucouleurs + exponential profile to determine the half-light radius $R_{1/2}$. We apply the Bell et al. (2003) mass-to-light ratio to the r –band flux and $g - r$ colors in this catalog to obtain an estimate for the total stellar mass M_* of every galaxy. We calculate two-point clustering w_p of our SDSS galaxy sample using line-of-sight projection of $\pi_{\text{max}} = 20\text{Mpc}$ using the **correl** program in **UniverseMachine**.

As the bedrock of our modeling, we use the catalog of **Rockstar** subhalos identified at $z = 0$ in the Bolshoi-Planck simulation (Klypin et al. 2011; Behroozi et al.

2013,?; Riebe et al. 2013; Rodríguez-Puebla et al. 2016). The particular version of the catalog we use is made publicly available through **Halotools** (Hearin et al. 2016), with `version_name = ‘halotools_v0p4’`.

We additionally explore the potential existence of satellite galaxies that reside in subhalos that are not identified by halo-finder to the present day, so-called “orphan galaxies” (see, e.g., Campbell et al. 2017). We use an extension of **Consistent Trees** that models the evolution of subhalos after disruption. The phase space evolution of orphans is approximated by following a point mass evolving in the host halo potential according to the orbital parameters of the subhalo at the time of disruption; the evolution of subhalo mass and circular velocity is approximated using the semi-analytic model presented in Jiang & van den Bosch (2014).

For mock galaxies, to compute galaxy clustering we employ the distant observer approximation by treating the simulation z –axis as the line-of-sight. We compute w_p using the `mock_observables.wp` function in **Halotools**, which is a python implementation of the algorithm in the **Corrfunc** C library (Sinha & Garrison 2017).

All numerical values of $R_{1/2}$ will be quoted in physical kpc, and all values of M_* and M_{halo} in M_\odot , assuming $H_0 = 67.8 \text{ km/s} \equiv 100h \text{ km/s}$, the best-fit value from

Planck Collaboration et al. (2016). To scale stellar masses to “ $h = 1$ units” (Croton 2013), our numerically quoted values for M_* should be multiplied by a factor of h^2 , while our halo masses and distances should be multiplied by a factor of h .

3 GALAXY-HALO MODEL

3.1 Stellar mass model

We map M_* onto subhalos with the best-fit stellar-to-halo mass relation from Moster et al. (2013):

$$\langle M_*/M_{\text{halo}} \rangle = 2N \left[(M_{\text{halo}}/M_1)^{-\beta} + (M_{\text{halo}}/M_1)^\gamma \right]^{-1}. \quad (1)$$

For halo mass M_{halo} we use M_{peak} , the largest value of M_{vir} ever attained along the main progenitor branch of the subhalo.

The values of the best-fit parameters in Moster et al. (2013) were fit to a stellar mass function (SMF) with values $M_*^{\text{MPA-JHU}}$ based on the MPA-JHU catalog (Kauffmann et al. 2003; Brinchmann et al. 2004), which differs from the SMF in our galaxy sample (see, e.g., Bernardi et al. 2014). We account for this difference by manually tabulating the median value $\langle M_*^{\text{Meert}+15} | M_*^{\text{MPA-JHU}} \rangle$ in logarithmic bins spanning $9 < \log_{10} M_*^{\text{MPA-JHU}}/M_\odot < 12$, and applying the median correction to the Monte Carlo realization of the mock galaxy sample. This results in a typical boost of ~ 0.25 dex at $M_*^{\text{MPA-JHU}} \approx 10^{9.75} M_\odot$, and ~ 0.4 dex at $M_*^{\text{MPA-JHU}} \approx 10^{11.5} M_\odot$.

3.2 Galaxy size models

In §4, we calculate predictions for the $R_{1/2}$ -dependence of galaxy clustering for several different kinds of empirical models, described in turn below.

3.2.1 M_* -only model

In the first class of models we explore, we suppose that stellar mass M_* is the statistical regulator of $R_{1/2}$, so that galaxy sizes are drawn from a log-normal distribution centered at $\langle R_{1/2} | M_* \rangle$, where M_* derives from the Moster et al. (2013) relation described above in §3.1. To implement this model, for simplicity we directly tabulate $\langle R_{1/2} | M_* \rangle$ from the data, rather than pursue a parametric form (see, e.g., Zhang & Yang 2017).

3.2.2 R_{vir} -only model

Motivated by Kravtsov (2013), we explore a model in which $R_{1/2}$ is linearly proportional to halo virial radius:

$$R_{1/2} = 0.0125 R_{\text{vir}} \quad (2)$$

For the virial radius of halos and subhalos, we use $R_{M_{\text{peak}}}$, the value of R_{vir} in physical units of kpc measured at the time of peak subhalo mass, defined by

$$M_{\text{peak}} \equiv \frac{4\pi}{3} R_{M_{\text{peak}}}^3 \Delta_{\text{vir}}(z_{M_{\text{peak}}}) \rho_m(z_{M_{\text{peak}}}), \quad (3)$$

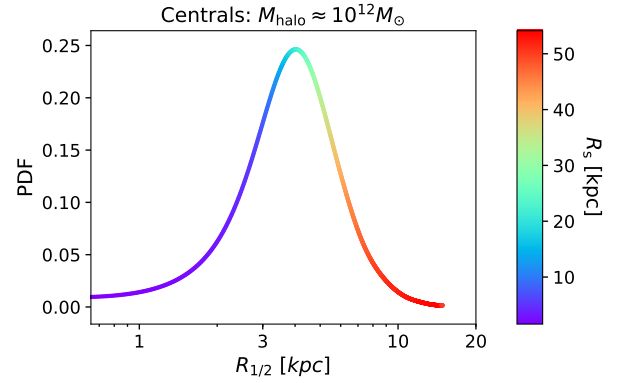


Figure 1. Profile co-evolution model. In this model, the log-normal distribution of galaxy sizes is determined by $R_{M_{\text{peak}}}$, the physical size of the halo virial radius at the time the halo reaches its peak mass. Thus log-normal the shape of this curve is determined by $\langle R_{1/2} | R_{M_{\text{peak}}} \rangle = 0.0125 R_{M_{\text{peak}}}$ with 0.2 dex of scatter. The profile co-evolution model further supposes that galaxy and halo profiles co-evolve across cosmic time. Thus within this log-normal distribution, for two halos with the same $R_{M_{\text{peak}}}$, halos with larger scale radius at $z_{M_{\text{peak}}}$ will host galaxies with above-average $R_{1/2}$, and conversely for halos with smaller values of $R_{s, M_{\text{peak}}}$.

where for $\Delta_{\text{vir}}(z_{M_{\text{peak}}})$ we use the fitting function to the “virial” definition used in Bryan & Norman (1998). For the model we refer to as the “ R_{vir} -only model”, we add uncorrelated log-normal scatter of $\sigma_{R_{1/2}} = 0.2$ dex to generate a Monte Carlo realization of the model population.

3.2.3 Profile co-evolution model

The “profile co-evolution” model is identical to the R_{vir} -only model, but the scatter in $R_{1/2}$ at fixed $R_{M_{\text{peak}}}$ is no longer purely stochastic, and is instead correlated with V_{peak} , defined as the value of V_{max} at $z_{M_{\text{peak}}}$. In this way, $R_{M_{\text{peak}}}$ statistically determines the distribution of available sizes, but halos with extended dark matter profiles and large scale radii R_s host galaxies with above-average sizes, while halos with small R_s host smaller galaxies. See Figure 1 for a visual illustration of this residual correlation. We implement scatter correlations using the `halotools.empirical_models.conditional_abunmatch` function, which generalizes the Conditional Abundance Matching technique described in Hearin et al. (2014).

3.2.4 M_* -stripping model

As we will show in §4, the chief ingredient needed to recover the observed clustering properties of galaxies is that satellites need to be smaller than centrals of comparable halo mass. Thus it is natural to consider a class of models in which stellar mass is stripped from satellite galaxies after infall.

The basis of this class of models is the fitting function presented in Smith et al. (2016), which was calibrated by studying stellar mass loss in a suite of high-resolution

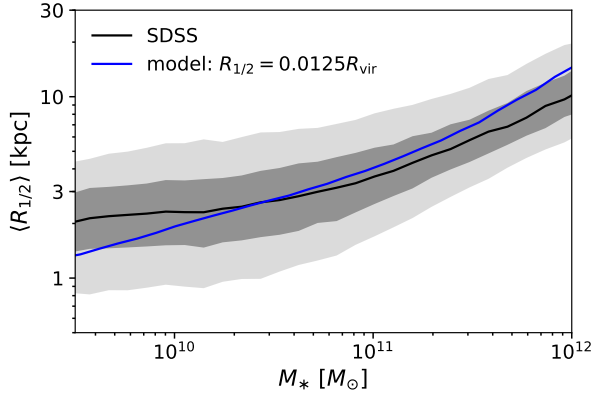


Figure 2. The black curve shows the median $R_{1/2} - M_*$ relation SDSS galaxies as measured in Meert et al. (2015). The two gray bands enveloping the black curve show the 50% and 90% percentile regions. The blue curve shows profile co-evolution model in which $\langle R_{1/2}|R_{\text{vir}} \rangle = 0.0125 R_{\text{vir}}$, as in Kravtsov (2013). This figure confirms that a linear relationship between R_{vir} and $R_{1/2}$, convolved against the nonlinear relationships between R_{vir} , M_{halo} and M_* , predicts the characteristic curvature in the relation $\langle R_{1/2}|M_* \rangle$ over a wide range in mass.

hydrodynamical simulations. In this model, f_* quantifies the fraction of stellar mass lost as a function of f_{DM} , the amount of dark matter that has been stripped since infall:

$$f_* = 1 - \exp(-14.2 f_{\text{DM}}) \quad (4)$$

For f_{DM} we use the ratio of present-day subhalo mass divided by the peak mass, $M_{\text{vir}}/M_{\text{peak}}$. If we denote the post-stripping stellar mass as M'_* , then we have $M'_* \equiv f_* M_*$, where M_* is given by Eq. 1. We then calculate the post-stripping radius by interpolating $\langle R'_{1/2}|M'_* \rangle$ directly from SDSS data.

4 RESULTS

In Figure 2 we show the scaling of galaxy size $R_{1/2}$ with M_* . The black curve enveloped by the gray bands show the scaling relation for our SDSS galaxy sample, while the blue curve shows the median relation $\langle R_{1/2}|M_* \rangle$ implied by the profile co-evolution model described in §3. This figure shows that models in which $R_{1/2} \propto R_{\text{vir}}$ can naturally give rise to the characteristic curvature in the $\langle R_{1/2}|M_* \rangle$ relation, confirming the results in Kravtsov (2013) in a forward modeling context.

4.1 Size-Dependent Clustering

In Figure 3 we present new measurements of the $R_{1/2}$ -dependence of projected galaxy clustering, $w_p(r_p)$. Because galaxy clustering has well-known dependence upon M_* that is not the subject of this work, we wish to remove this influence and focus purely on the relationship between $R_{1/2}$ and $w_p(r_p)$. To do so, we determine the value $\langle R_{1/2}|M_* \rangle$ by computing a sliding median of $R_{1/2}$, calculated using a window of width $N_{\text{gal}} = 1000$. Each galaxy is categorized as either “large” or “small”

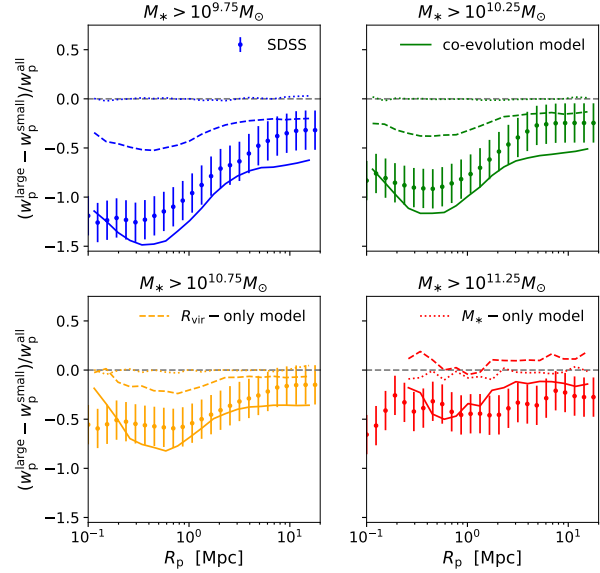


Figure 3. $R_{1/2}$ -dependence of galaxy clustering. Points with error bars show new SDSS measurements of the $R_{1/2}$ -dependence of projected galaxy clustering, w_p . We define a galaxy as “large” or “small” according to whether it is above or below the median size for its stellar mass, so that in each panel, the stellar mass functions of the “large” and “small” subsamples are identical, as described in the text. The y-axis shows *clustering strength ratios*, so that, for example, a y-axis value of -0.5 corresponds to small galaxies being 50% more strongly clustered than large galaxies of comparable stellar mass. Each panel shows results separately for different volume-limited M_* -threshold samples; predictions of three different models are shown in each panel. See §3.2 for a description of each model.

according to whether it is above or below the median value appropriate for its stellar mass. Using this technique, we stress that for any M_* -threshold sample, the SMF of the “large” and “small” subsamples are identical, by construction.

We measure $w_p(r_p)$ separately for large and small subsamples for four different M_* thresholds, $M_* > 10^{9.75} M_\odot$, $M_* > 10^{10.25} M_\odot$, $M_* > 10^{10.75} M_\odot$, and $M_* > 10^{11.25} M_\odot$. We make the same measurements for each volume-limited M_* -threshold sample *without* splitting on size, giving us measurements w_p^{all} , w_p^{large} , and w_p^{small} for each threshold sample. This allows us to compute the ratio $(w_p^{\text{large}} - w_p^{\text{small}})/w_p^{\text{all}}$, which we refer to as *the $R_{1/2}$ clustering ratio*. These ratios are the measurements appearing on the y-axis in each panel of Figure 3. Points with jackknife-estimated error bars show SDSS measurements, solid curves show the clustering ratios of model galaxies as predicted by the models described in §3.

The salient feature of the clustering ratio measurements is that they are negative: small galaxies cluster more strongly than large galaxies of the same stellar mass, a new result. This feature also holds true for galaxies predicted by the R_{vir} -only model. This result may be surprising, since $R_{1/2} \propto R_{\text{vir}}$, halo mass $R_{\text{vir}} \propto M_{\text{halo}}^{1/3}$, and clustering strength increases with M_{vir} . Based on this

simple argument, one would expect the opposite trend to the measurements shown here.

4.2 Central vs. Satellite Sizes

A straightforward resolution to the above puzzle is shown in Figure 4, which compares the $R_{1/2}$ distributions of central, satellite, and splashback galaxies with the same halo mass $M_{\text{peak}} \approx 10^{12} M_{\odot}$. A “splashback” galaxy is defined as a present-day central that used to be a satellite, i.e., its main progenitor halo passed inside the virial radius of a larger halo at some point in its past history. On the other hand, we define a “true central” as a galaxy that has never been a satellite.

In the R_{vir} -only model, satellite and splashback galaxies are smaller than centrals of the same halo mass due to the physical size of their halo being smaller at earlier times $z_{M_{\text{peak}}}$. There are two distinct reasons why this feature results in small galaxies being more strongly clustered relative to larger galaxies of the same mass. First, satellite galaxies statistically occupy higher mass host halos that are more strongly clustered. In models where satellites are smaller than centrals, for any given M_* -threshold the “small” subsample will naturally have a higher satellite fraction, resulting in a negative clustering ratio as seen in SDSS data. Second, at fixed mass, halos of L_* galaxies that form earlier are more strongly clustered, a phenomenon commonly known as *halo assembly bias*. Since splashback halos are typically earlier forming than true centrals, then models where splashback halos host smaller-than-average galaxies will naturally predict negative clustering ratios.

In the M_* -only model, in which $R_{1/2}$ is statistically set by present-day stellar mass with no other dependencies. Thus neither of the above features are present: satellites and centrals of the same mass have no differences in size, and there is essentially no $R_{1/2}$ -dependence to galaxy clustering, in gross disagreement with our SDSS observations.

Much more successful is the profile co-evolution model shown with the solid curves in Figure 3. The strongly negative clustering ratios predicted by the assumption of profile co-evolution can be understood in terms of the same features discussed above. Figure 1 shows that at fixed M_{peak} , larger galaxies will occupy halos with larger $R_{\text{s}, M_{\text{peak}}}$. Since halo concentration $c = R_{\text{vir}}/R_{\text{s}}$, this implies that high-concentration galaxies will tend to host smaller galaxies. Both satellites and splashback centrals have higher concentration than true centrals, another manifestation of assembly bias, and so the assumption of profile co-evolution naturally results in an enhancement of the clustering ratios beyond the R_{vir} -only model.

4.3 Tidal Stripping and Orphan Satellites

We conclude this section with a discussion of Figure 5, which provides an estimate of how satellite mass stripping and orphan galaxies impact size-dependent clustering ratios. In the M_* -stripping model described in §3.2.4, satellites lose stellar mass in a way that mimics what is

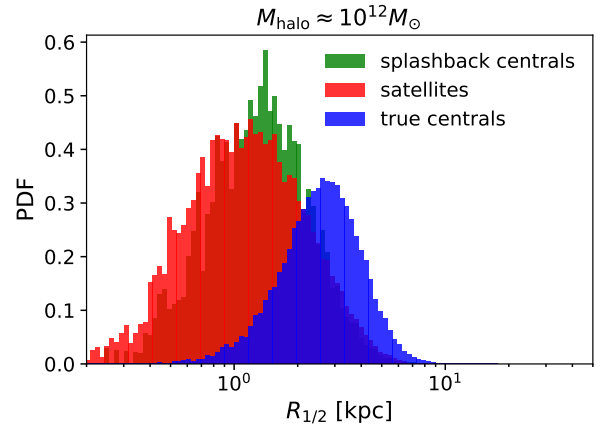


Figure 4. Relative sizes of centrals and satellites. In a narrow bin of halo mass $M_{\text{halo}} = M_{\text{peak}} \approx 10^{12} M_{\odot}$, we show the distribution of model galaxy sizes for different subpopulations galaxies, as predicted by the R_{vir} -only model. The red histogram shows the sizes of satellites; the blue histogram shows host halos that have never passed inside the virial radius of a larger halo (“true centrals”); the green histogram host halos that were subhalos inside a larger at some point in their past history (“splashback halos”). In the R_{vir} -only model, galaxy size is set by the *physical* size of the virial radius at the time the halo attains its peak mass, naturally resulting in smaller sizes for satellites and backplash centrals relative to true centrals of the same M_{peak} . The central/satellite size differences shown here are not enough to correctly predict the observed clustering ratios (see Figure 3), motivating the M_* -stripping and profile co-evolution models.

seen in high-resolution hydrodynamical simulations. This naturally results in an enhancement of size differences between satellites and centrals, and the dot-dashed curves in Figure 5 show that produces the expected sign of the effect on the clustering ratios. The magnitude of the effect, however is not strong enough to remedy the discrepancy of the clustering predictions of the R_{vir} -only model. We discuss the physical implications of this result in §5.3.

The dotted curves in Figure 5 show results of the R_{vir} -only model applied to a subhalo catalog that includes a orphan halos. As described in §??, orphan halos are subhalos that are no longer resolved by *Rockstar*, but whose evolution is tracked in a post-processing phase. We apply the same mass-stripping model described in §3.2.4 to this subhalo catalog that includes orphan halos, keep all model galaxies that retain more than half of their stellar mass, and show results for the R_{vir} -only model applied to the resulting catalog.

As the orphan catalog has a higher satellite fraction than the standard subhalo catalog, the negative boost shown the dotted curves in Figure 5 is expected. Orphan halos also typically have earlier-than-average values of $z_{M_{\text{peak}}}$ relative to ordinary subhalos, which also enhances differences between central and satellite sizes. See §5.3 for further discussion.

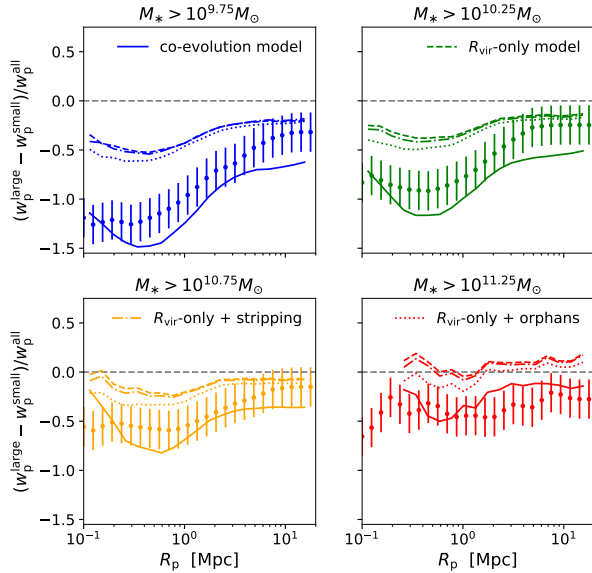


Figure 5. Impact of tidal stripping and orphan satellites. In all panels, the axes and points with error bars are the same as in Figure 3. The dashed curves (“ R_{vir} -only model”) and solid curves (“profile co-evolution model”) from Figure 3 are also shown for convenience. The dot-dashed curves show results for a model in which satellites lose mass after infall in a manner similar to what is seen in high-resolution hydrodynamical simulations, as described in §3.2.4. The dotted curve shows results for the same model, but including the effect of “orphan” galaxies that live in subhalos no longer resolved by Rockstar.

5 DISCUSSION

5.1 Progression from Backward to Forward Modeling

Our results give an archetypal demonstration of the natural scientific progression from backward to forward modeling. In backward modeling, some mapping is applied to observed galaxies to estimate the values of model quantities such as halo mass. In Kravtsov (2013), the model quantities mapped onto galaxies are M_{halo} and R_{vir} ; another classic example of backward modeling uses a group- or cluster-finding algorithm to assign M_{halo} to observed galaxies (e.g., Berlind et al. 2006; Yang et al. 2005; Rykoff et al. 2014). Once the observed galaxies have been supplemented with model variables, then the relations of the galaxy-halo connection can be inferred, for example, by calculating quantities such as the mean stellar mass or quiescent fraction as a function of halo mass (e.g., Yang et al. 2005; Weinmann et al. 2006).

In forward modeling, the direction of inference is turned around: a mapping is instead applied to the model quantities such as M_{halo} . In the case of *Halotools*, this transforms a cosmological simulation into a synthetic galaxy catalog that can be directly compared with observations. This enables a richer quantitative study of modeling hypotheses relative to backward modeling. For example, Figure 3 shows how forward modeling allows us to exploit galaxy clustering measurements to quantitatively test whether M_{halo} or M_* is the statistical regulator

of galaxy size. The ability disentangle coupled variables such as M_* and M_{halo} is just one example of this advantage of forward modeling. Another example is illustrated in Figure 4, in which we explore the role of splashback halos in setting galaxy size. In our forward modeling approach, this is entirely straightforward; in backward modeling, such an investigation would not even be possible without introducing additional modeling ingredients.

Backward modeling the galaxy-halo connection is useful for generating hypotheses and motivating functional forms. Forward modeling becomes necessary when the problem at hand becomes encumbered by multiple relevant variables, as is the case with galaxy size. Forward modeling also makes it possible to conduct rigorous Bayesian inference, which we consider to be the next natural step in the progression described here (see §5.4 for further discussion).

5.2 Empirical Modeling $R_{1/2}$: advantages and limitations

5.3 Implications for Satellite Mass Loss

5.4 Future Directions for Empirical Modeling of Morphology

6 CONCLUSIONS

6.1 Summary

ACKNOWLEDGMENTS

APH thanks John Baker for the *Toejam & Earl* soundtrack.

REFERENCES

- Ahn C. P., Alexandroff R., Allende Prieto C., Anders F., Anderson S. F., Anderton T., Andrews B. H., Aubourg É., Bailey S., Bastien F. A., et al. 2014, *ApJS*, 211, 17
- Behroozi P. S., Wechsler R. H., Wu H.-Y., 2013, *ApJ*, 762, 109
- Behroozi P. S., Wechsler R. H., Wu H.-Y., Busha M. T., Klypin A. A., Primack J. R., 2013, *ApJ*, 763, 18
- Bell E. F., McIntosh D. H., Katz N., Weinberg M. D., 2003, *ApJS*, 149, 289
- Berlind A. A., Frieman J., Weinberg D. H., et al., 2006, *ApJS*, 167, 1
- Bernardi M., Meert A., Sheth R. K., Vikram V., Huertas-Company M., Mei S., Shankar F., 2013, *MNRAS*, 436, 697
- Bernardi M., Meert A., Vikram V., Huertas-Company M., Mei S., Shankar F., Sheth R. K., 2014, *MNRAS*, 443, 874
- Brinchmann J., Charlot S., White S. D. M., Tremonti C., Kauffmann G., Heckman T., Brinkmann J., 2004, *MNRAS*, 351, 1151
- Bryan G. L., Norman M. L., 1998, *ApJ*, 495, 80
- Campbell D., van den Bosch F. C., Padmanabhan N., Mao Y.-Y., Zentner A. R., Lange J. U., Jiang F., Villarreal A., 2017, *ArXiv:1705.06347*
- Croton D. J., 2013, *PASA*, 30, e052

- Hearin A., Campbell D., Tollerud E., et al., 2016, ArXiv e-prints
- Hearin A. P., Watson D. F., Becker M. R., Reyes R., Berlind A. A., Zentner A. R., 2014, MNRAS , 444, 729
- Jiang F., van den Bosch F. C., 2014, ArXiv e-prints
- Kauffmann G., Heckman T. M., White S. D. M., et al., 2003, MNRAS , 341, 33
- Klypin A. A., Trujillo-Gomez S., Primack J., 2011, ApJ , 740, 102
- Kravtsov A. V., 2013, ApJL , 764, L31
- Meert A., Vikram V., Bernardi M., 2013, MNRAS , 433, 1344
- Meert A., Vikram V., Bernardi M., 2015, MNRAS , 446, 3943
- Moster B. P., Naab T., White S. D. M., 2013, MNRAS , 428, 3121
- Planck Collaboration Ade P. A. R., Aghanim N., Arnaud M., Ashdown M., Aumont J., Baccigalupi C., Banday A. J., Barreiro R. B., Bartlett J. G., et al. 2016, AAP, 594, A13
- Riebe K., Partl A. M., Enke H., Forero-Romero J., Gottlöber S., Klypin A., Lemson G., Prada F., Primack J. R., Steinmetz M., Turchaninov V., 2013, Astronomische Nachrichten, 334, 691
- Rodríguez-Puebla A., Behroozi P., Primack J., Klypin A., Lee C., Hellinger D., 2016, MNRAS , 462, 893
- Rykoff E. S., Rozo E., Busha M., et al., 2014, ApJ , 785, 104
- Sinha M., Garrison L., , 2017, Corrfunc: Blazing fast correlation functions on the CPU, Astrophysics Source Code Library
- Smith R., Choi H., Lee J., Rhee J., Sanchez-Janssen R., Yi S. K., 2016, ApJ , 833, 109
- Vikram V., Wadadekar Y., Kembhavi A. K., Vijayagovindan G. V., 2010, MNRAS , 409, 1379
- Weinmann S. M., van den Bosch F. C., Yang X., Mo H. J., 2006, MNRAS , 366, 2
- Yang X., Mo H. J., Jing Y. P., van den Bosch F. C., 2005, MNRAS , 358, 217
- Yang X., Mo H. J., van den Bosch F. C., Jing Y. P., 2005, MNRAS , 356, 1293
- Zhang Y., Yang X., 2017, ArXiv e-prints